Journal of Energy Storage 106 (2025) 114698

Contents lists available at ScienceDirect

Journal of Energy Storage

journal homepage: www.elsevier.com/locate/est

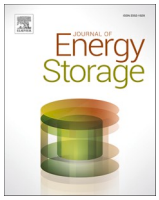

Research papers

Exploring the effect of magnesium oxide on electrochemical properties of polypyrrole encapsulated on graphitic carbon nitride for supercapacitors applications

Manisha [a], Monika Dhanda [b], Varij Panwar [c], Suman Lata [b], Harish Kumar [d], Anshu Sharma [e,*]

[a] Department of Physics and Astrophysics, School of Basic Sciences, Central University of Haryana, Mahendragarh 123031, India
[b] Department of Chemistry, Deenbandhu Chhotu Ram University of Science and Technology, Murthal 131039, Haryana, India
[c] Department of Electronics and Communication Engineering, Graphic Era (Deemed to be University), Dehradun 248002, Uttarakhand, India
[d] Department of Chemistry, School of Basic Sciences, Central University of Haryana, Mahendragarh 123031, India
[e] Department of Applied Sciences and Humanities, School of Engineering & Technology, Central University of Haryana, Mahendragarh 123031, India

ARTICLE INFO

Keywords:
Magnesium oxide/graphitic carbon nitride/ Polypyrrole
Electrochemical measurement
Electrode material
Supercapacitor

ABSTRACT

This study addresses the facile synthesis of magnesium oxide/graphitic carbon nitride/Polypyrrole (MGP) composites by varying the concentration of magnesium oxide. These composites were synthesized via calcination route followed by in-situ polymerization reaction thus naming the composites as MGP0.5, MGP1, MGP2 and MGP3. The structural analysis of composites is done through X-ray diffraction (XRD), Fourier Transform Infrared Spectroscopy (FTIR) and Raman spectroscopy while the morphology is analyzed through Field Emission Scanning Electron Microscopy (FESEM) and supported by Transmission Electron Microscopy (TEM). The MGP2 composite, assessed through multi-point BET theory, exhibits a specific surface area of 109.45 $m^2 g^{-1}$, surpassing that of its precursor materials. This enhanced surface area facilitates a greater number of active sites for the adsorption-desorption of ions. The assessment of electrochemical properties is done through cyclic voltammetry (CV), galvanostatic charge discharge (GCD) and electrochemical impedance spectroscopy (EIS) in three-electrode setup in 1 M H_2SO_4 which delivers a specific capacitance of 1132.12 F g^{-1} at 5 mV s^{-1} for MGP2 composite. The practical applicability of the electrode material was examined by fabricating an asymmetric supercapacitor device which delivers an energy density of 9.25 W h kg^{-1} at a power density of 302.72 W kg^{-1}. The supercapacitor device exhibited 94.03 % capacitance retention after 10,000 cycles demonstrating its potential to be used as a future supercapacitor applications.

1. Introduction

With increasing human population, energy demand is increasing leading to the increased consumption of fossil fuels which is directly linked to the problems like global warming and climate change [1]. These challenges can be mitigated through the substitution of fossil fuels with sustainable energy sources, including wind power, solar radiation harnessing, and geothermal heat extraction. But the generation of energy from these sources is highly dependent on geographical and environmental factors so development of efficient energy storage devices is essential for the exploitation of these sources [2,3]. In recent years, supercapacitors (SCs) have garnered significant attention because of their quick charging-discharging process, high power density and environment friendliness [4,5]. However, the energy density of SCs imposes constraints on their applicability in commercial applications [6–8]. Supercapacitors exhibit elevated energy density in comparison to electrolytic capacitors and boast higher power density relative to batteries, effectively serving as a transitional link between electrolytic capacitors and batteries. But their charge storage mechanism resembles more with batteries than electrolytic capacitors [9,10].

The fundamental constituents of a SC are electrode material, an electrolyte, a separator and a current collector. The evaluation of its efficacy entails quantifying its energy density, a pivotal metric for assessing the storage capacity of electrical energy per unit mass [11]. Energy density of SC directly depends on its capacitance and exhibits a proportionality to the square of applied voltage. Therefore, elevating the specific capacitance of an SC can lead to an increase in its energy density, a factor that is predominantly influenced by the selection of the

* Corresponding author.
E-mail address: anshushsharda@gmail.com (A. Sharma).

https://doi.org/10.1016/j.est.2024.114698
Received 7 June 2024; Received in revised form 13 November 2024; Accepted 17 November 2024
Available online 29 November 2024

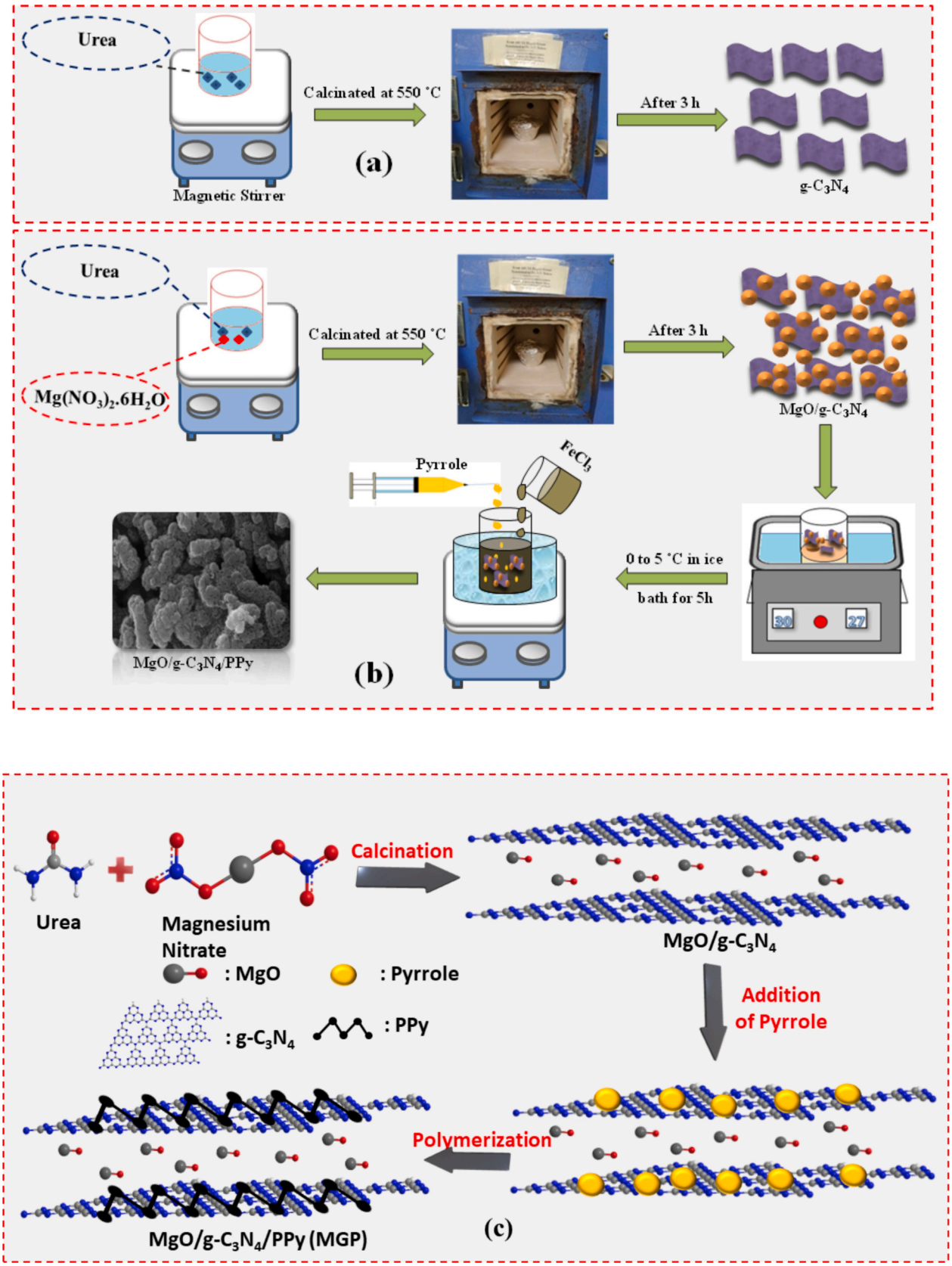

Fig. 1. Schematic illustration of the synthesis process of (a) g-C_3N_4 (b) MGP composites (c) Schematic of synthesis in structural form.

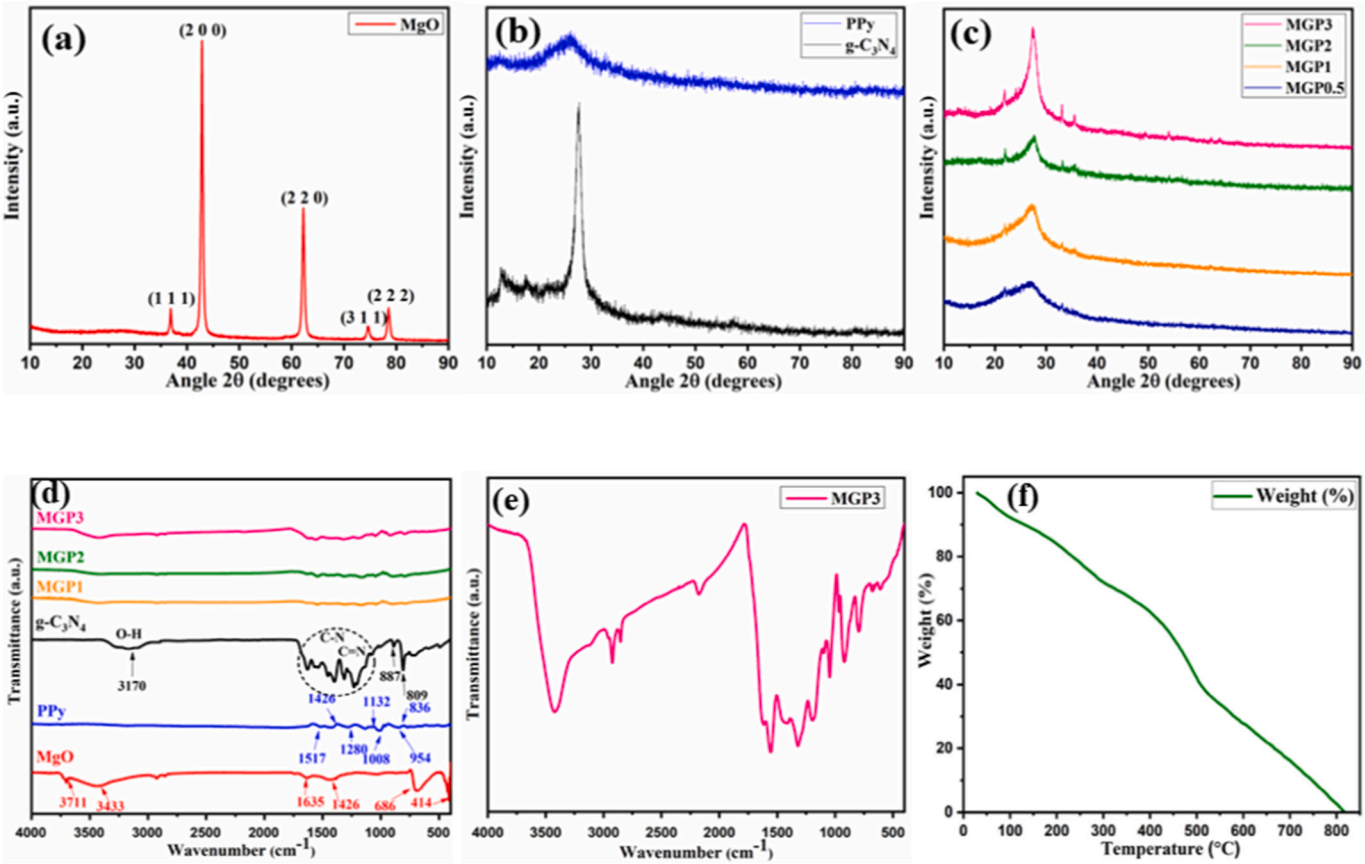

Fig. 2. XRD pattern of (a) MgO (b) g-C_3N_4, PPy (c) MGP composites (d) FTIR spectra of MgO, g-C_3N_4, PPy and MGP composites (e) FTIR spectra of MGP3 (f) Variation of weight percentage with temperature for MGP2 composite.

electrode material [12,13]. Conductive polymers exhibit high values of specific capacitance because of the involvement of fast faradic reactions but their low cyclic stability curb their use. Dubal et al. fabricated PPy nanosheets and obtained a specific capacitance of 586 F g^{-1} at 2 mV s^{-1} in 0.5 M H_2SO_4 [14]. Zhu et al. synthesized Polyaniline (PANI) via oxidative polymerization and obtained a specific capacitance of 302.43 F g^{-1} in 1 M HCl [15]. Xu et al. synthesized PPy modified iron oxide nanocomposites via hydrothermal technique and obtained a very high cyclic stability of 97.3 % after 20,000 cycles [16]. Fan et al. synthesized PANI-Co_3O_4 composites by hydrothermal and polymerization reaction and the specific capacitance was retained 74.81 % after 3000 cycles [17]. Furthermore, enhancements in electrochemical characteristics were observed in binary and ternary composites comprising carbon derivatives, metal oxides/sulfides, and polymers. For instance, Zhang et al. synthesized composite material comprising of PPy and graphene through in-situ polymerization reaction and obtained a impressive 96 % capacitance retention for composite after 1000 cycles while pure PPy exhibited a mere 64 % capacitance under same conditions. Additionally, the specific capacitance observed an enhancement from 152 F g^{-1} for pure PPy to 482 F g^{-1} for graphene/PPy at 0.5 A g^{-1} [18]. Aphale et al. synthesized freestanding electrode of Graphene/CNT/PPy and obtained ultrahigh energy density of 62.96 W h kg^{-1} [19]. Moyseowicz et al. combined PPy wfith Fe_2O_3/reduced graphene oxide and observed a 70 % higher capacitance because of the insertion of PPy [20].

In recent developments, there has been a thriving interest in exploring the potential of magnesium for supercapacitors through the doping of transition metals such as vanadium [21] and also by using it to synthesize porous CNTs [22]. Because of the low cost and eco friendliness, magnesium is being used in variety of applications such as refractory materials and superconductors but the wide band gap of magnesium oxide (5 eV to 8 eV) limits its direct usage as an electrode material [23]. Further, metal doping in layered structure such as g-C_3N_4 increases its electrical, optical and electrochemical properties by tuning its valence band and conduction band [24]. In this work, we have added magnesium oxide (MgO) in a lower band gap material like g-C_3N_4 (2.7 eV) which possesses the properties of electrode material like high specific surface area, high stability and is conductive in nature but has lower value of specific capacitance [25,26]. Further enhancement in electrochemical performance is possible by synthesizing its composite with a conducting polymer like PPy which is easy to synthesize, has virtuous electronic conductivity and has high value of specific capacitance [27,28].

In light of the above mention facts, we have, for the first time, synthesized a ternary composite of MgO, g-C_3N_4 and PPy by simple in-situ polymerization reaction followed by calcination route. The novelty of this work lies in using this composite as an electrode material for supercapacitors. Furthermore, the electrochemical performance of electrode material was systematically enhanced by modulating the content of MgO.

2. Experimental

2.1. Chemicals

Magnesium Nitrate Hexahydrate ($Mg(NO_3)_2.6H_2O$), Sulfuric acid and Polyvinyl Alcohol (PVA) were purchased from Sigma Aldrich. Ferric Chloride Anhydrous ($FeCl_3$) and pyrrole were purchased from Chemical Drug House (CDH). Urea and Dimethylformamide (DMF) were obtained from Thermo Fischer Scientific. All chemicals and reagents were of analytical grade and pyrrole monomer was distilled before use.

2.2. Synthesis of magnesium oxide (MgO)

5 g of $Mg(NO_3)_2.6H_2O$ was dissolved in 10 ml distilled water (DW), after that the resulting solution was subjected to desiccation in a hot air oven operating at 80 °C. Thereafter this dried sample was transferred to alumina crucible which was covered with foil and subsequently positioned within a muffle furnace. The muffle furnace temperature was gradually increased up to 550 °C at a controlled rate of 2 °C min^{-1} and maintained at 550 °C for 3 h. At this temperature $Mg(NO_3)_2.6H_2O$ decompose to give magnesium oxide and releases nitrogen dioxide (NO_2) and oxygen gas (O_2) [29].

2.3. Synthesis of graphitic carbon nitride (g-C_3N_4)

The synthesis of g-C_3N_4 was achieved through the transformation of urea. This was accomplished by dissolving 10 g urea in 20 ml DW subsequently subjecting the resulting solution to drying in hot air oven. Following this, the dried sample was carefully transferred into an alumina crucible, covered with an aluminium foil, and subsequently placed within a muffle furnace. The muffle furnace temperature was systematically raised up to 550 °C at a controlled ramp rate of 2 °C min^{-1} where it was maintained for 3 h [30].

2.4. Synthesis of MgO/g-C_3N_4/PPy composites

x mmol of $Mg(NO_3)_2.6H_2O$ (where x = 0.5, 1, 2, 3) and 10 g of urea were dissolved in 40 ml of DW while stirring. After drying the solution in hot air oven, it was calcinated at 550 °C for 3 h. Resultant sample was crushed with mortar pestle to obtain final MgO/g-C_3N_4 (MG) composite [31]. Thereafter, 0.4 g of MG composite was subjected to ultrasonication with 30 ml of methanol for a duration of 2 h. The resulting mixture was further incorporated to well mixed solution of DW and methanol (1:2). Subsequently, 0.5 ml pyrrole solution were introduced to this. Then, to initiate the polymerization reaction, freshly prepared 0.1 M $FeCl_3$ solution was added dropwise. This reaction was proceeded for 5 h within an ice bath. After this, the solution was refrigerated overnight and subjected to filtration through Whatman filter paper. After thorough washing of the precipitates with methanol and DW, they were dried in an oven maintained at 80 °C. A schematic illustration of this synthesis process is presented in Fig. 1.

2.5. Characterizations

2.5.1. Structural analysis

To conduct structural analysis on the synthesized materials, X-ray diffraction patterns were obtained utilizing a Rigaku SmartLab setup, employing X-rays with a wavelength of 1.54 A^0. The X-ray diffraction pattern was recorded between 10^0 and 90^0 at the rate of 2 ^{0} min^{-1}. The XRD of Magnesium oxide showed the peaks at 36.90^0, 42.88^0, 62.22^0, 74.62^0 and 78.76^0 which matches accurately with the peaks of MgO nanoparticles (JCPDS No. 75–0447) confirming the proper synthesis of nanoparticles (Fig. 2(a)) [32]. PPy has a broad peak around 26^0 representing the formation of polymer chain while the broadness of peak reveals the amorphous nature of polymer chain. g-C_3N_4 has two characteristic peaks at 13.1^0 and 27.6^0 demonstrating planes (100) and (002) respectively (Fig. 2(b)) which confirms the in-plane structural packing of g-C_3N_4 with periodic arrangement of layers [33]. As the concentration of MgO was increased in MGP composites, the intensity of peak at 27.6^0 increased and the peak became narrower revealing the transformation from amorphous to semi crystalline nature of MGP composites. Small peaks of magnesium oxide were also observed in MGP2 and MGP3 composites confirming the synthesis of MGP composites (Fig. 2 (c)).

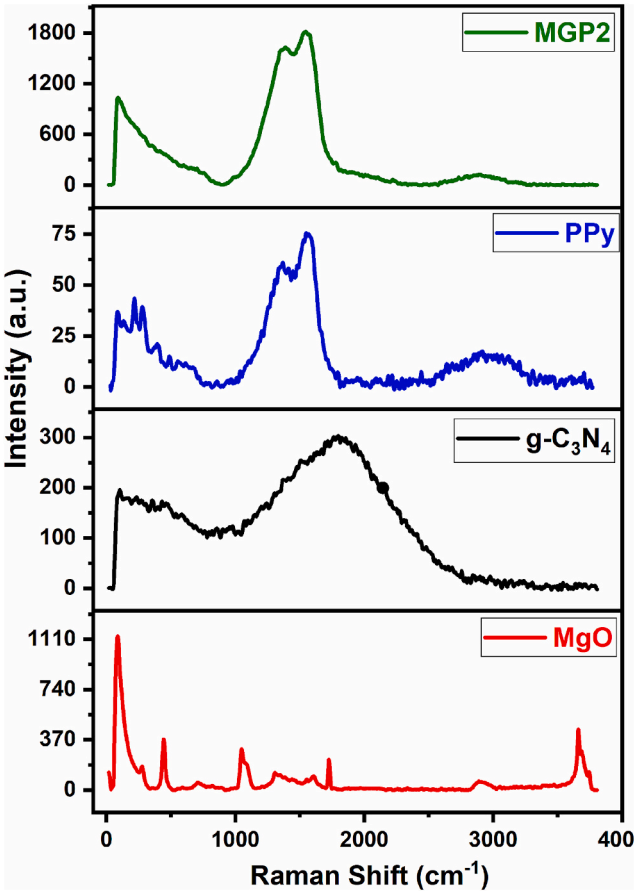

Fig. 3. Raman spectra of MgO, g-C_3N_4, PPy and MGP2 composite.

2.5.2. Fourier Transform Infrared Spectroscopy (FTIR)

FTIR spectra was obtained to analyze the chemical composition and functional groups present in the sample using Perkin Elmer Spectrum, BX II. Fig. 2(d) demonstrates the FTIR spectra of MgO, g-C_3N_4, PPy and MGP composites. The transmittance peak ranging from 1200 cm^{-1} to 1640 cm^{-1} in the spectrum of g-C_3N_4 corresponds to the stretching vibrations of C—N and C═N bonds within the aromatic ring structure. Additionally, the distinctive bands at 809 cm^{-1} and 887 cm^{-1} affirm the presence of out-of-plane vibrations associated with the tri-*s*-triazine ring [34]. In FTIR spectra of PPy, the observed bands at 1517 cm^{-1} and 1426 cm^{-1} are attributed to the fundamental ring vibrations inherent to PPy. Furthermore, the band appearing at 1132 cm^{-1} corresponds to the stretching vibrations of C—N bond. Additionally, the transmittance bands at 1280 cm^{-1} and 1008 cm^{-1} signify the deformations involving the C=C-N ring and the in-plane bending of C—H bonds within the ring structure, respectively [35]. The bands appearing below 1000 cm^{-1} in the spectra of MgO are related to Mg—O bond. MgO readily absorbs water molecules from atmosphere which is confirmed by the band at 1635 cm^{-1} [36]. From Fig. 2(e), it can be perceived that FTIR spectra of MGP3 resembles with those of its predecessors with some shift in frequency confirming the presence of g-C_3N_4, PPy and MgO in the composite. In addition, the band appearing at 2172 cm^{-1} corresponds to the N-C-N vibrations which arises due to the interaction between Mg atom of MgO and N atom of g-C_3N_4 [37]. The small peak at 2923 cm^{-1} in FTIR spectra of MgO and MGP3 might be attributed to the O—H bonding resulting from the absorption of moisture [38].

2.5.3. Thermo gravimetric gnalysis (TGA)

For the assessment of sample thermal stability and decomposition behavior, TGA was conducted using TGA HiRes1000 within a nitrogen

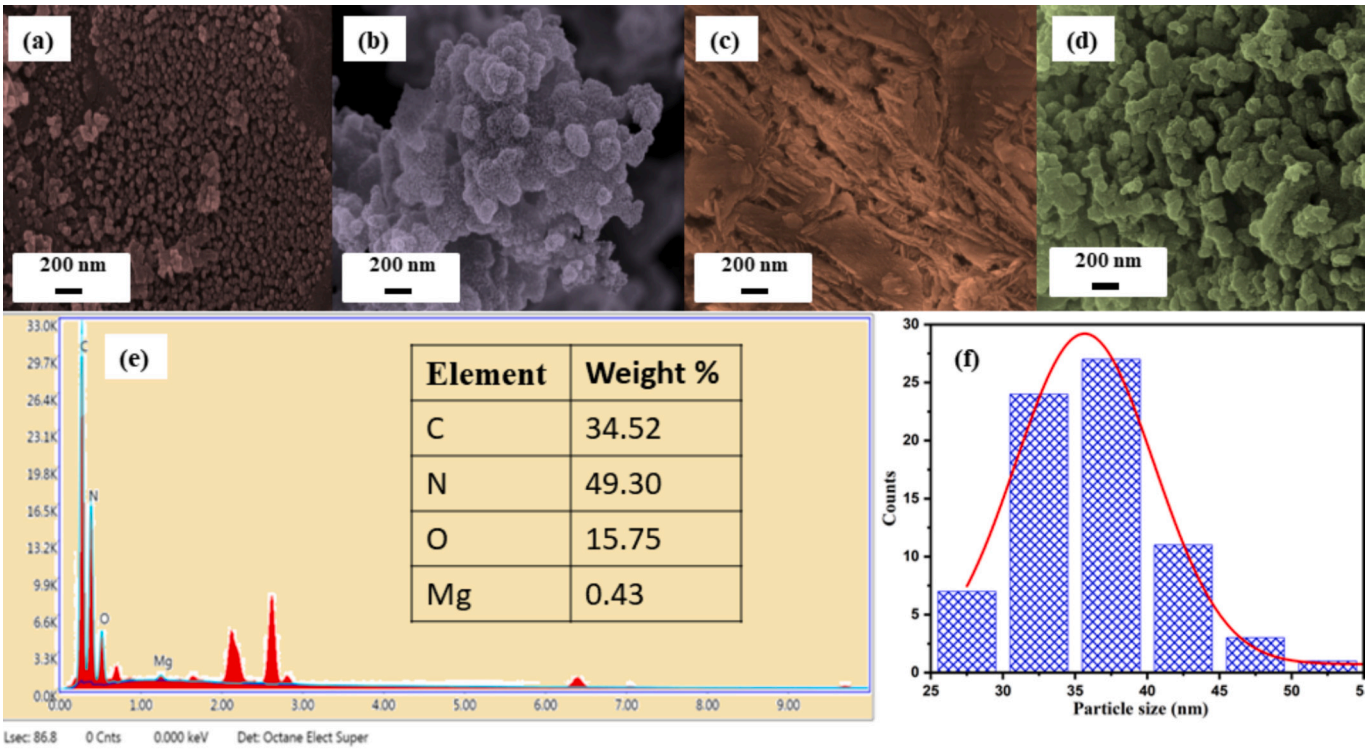

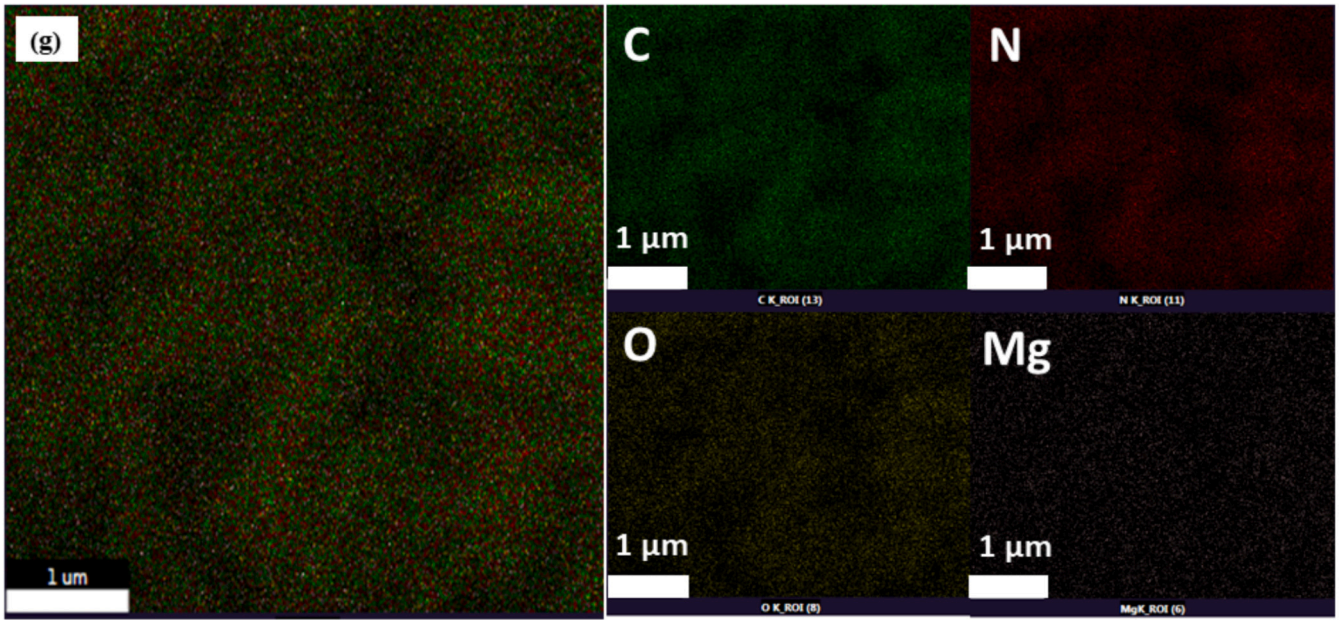

Fig. 4. FESEM images of (a) MgO (b) PPy (c) g-C_3N_4 (d) MGP2 (e) Energy dispersive spectra of MGP2 (f) Histogram plot for calculating size of MgO particles (g) Elemental mapping image of MGP2 composite.

atmosphere. The temperature was incrementally increased from 30 °C to 900 °C at the rate of 4 ^{0} min^{-1}. Fig. 2(f) depicts the relationship between temperature and weight loss of MGP2 composite. There is a linear weight loss of 30 % till 320 °C which suggests the removal of moisture and other volatile impurities. Up to 475 °C, 50 % of weight loss was observed which may be attributed to the breakdown of chemical bonds and decomposition of PPy chain. After that, there is again a linear weight loss which suggests a continuous process of decomposition and might be due to the breakdown of g-C_3N_4 into carbon and nitrogen containing gases. Thus, the MGP composite shows its stability till 475 °C confirming the presence of PPy and g-C_3N_4.

2.5.4. *RAMAN spectroscopy*

To further get some more insight about the molecular vibrations specifically π conjugated systems, Raman spectroscopy was conducted using a laser with a wavelength of 632 nm using WITec employing Alpha300 model. Based on the data presented in Fig. 3, the Raman spectrum reveals specific vibrational modes of interest. The band

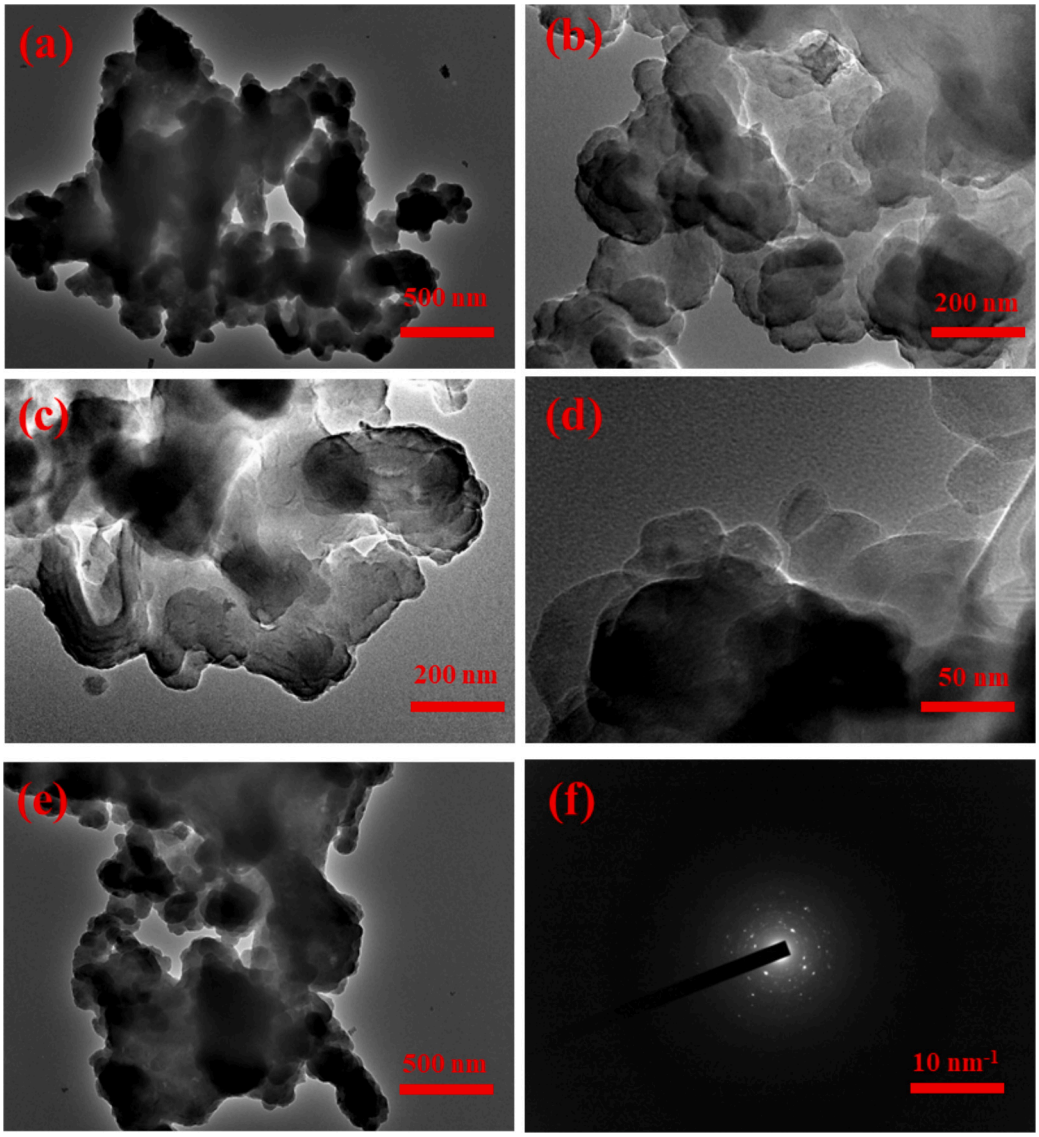

Fig. 5. HR-TEM images of MGP2 composite at (a) 500 nm (b) 200 nm (c) 200 nm (d) 50 nm (e) 500 nm (f) SAED pattern of MGP2 composite.

observed at 1366 cm^{-1} corresponds to the in-plane bending vibrations associated with the carbon-hydrogen (C—H) bonds within the PPy ring structure. Conversely, the presence of carbon-carbon double bonds (C=C) in the PPy ring is confirmed by the band detected at 1557 cm^{-1} [39]. The broad band around 3000 cm^{-1} is associated with the stretching vibrations of C—H bond. Raman spectra of MgO shows peaks around 446 cm^{-1}, 1073 cm^{-1} which confirms the formation of MgO nanoparticles and the peaks at 3660 cm^{-1} and 2920 cm^{-1} might be due to the absorbed moisture from the environment to transform into Mg $(OH)_2$ [38]. The Raman spectra of g-C_3N_4 demonstrates a wide band around 1800 cm^{-1} indicative of stretching vibrations within the triazine ring. In Raman spectra of MGP2 composite, the intensity of D band (disorder band) and G band (graphitic band) increased many folds depicting that the incorporation of MgO and g-C_3N_4 has a significant impact on the π conjugated structure and interaction within the PPy matrix. Enhanced π-π stacking interactions could potentially improve the charge transport characteristics of the composite material, thereby rendering it a promising candidate for utilization as an electrode material for energy storage applications.

2.5.5. Morphological analysis

To examine the morphology of synthesized samples, Field Emission Scanning Electron Microscopy with Energy Dispersive X-ray (EDX) and elemental mapping was performed by Zeiss GeminiSEM 500 Thermal field emission type microscope at an acceleration voltage of 30 kV. The morphology of samples is demonstrated in Fig. 4(a-d). It was observed that magnesium oxide has spherical shape with average particle size of 35 nm. As a result of the incorporation of MgO, g-C_3N_4 and PPy, the morphology of MGP composite has been modified, displaying a transformed globular structure reminiscent of the altered configuration of PPy. These morphological modifications with increased fluffiness are expected to impart smooth flow of charge between electrode and electrolyte resulting in better charge storage. The elemental composition of composite determined through EDX was found to be 34.52 %, 49.30 %, 15.75 % and 0.43 % for carbon (C), nitrogen (N), oxygen (O) and magnesium (Mg) respectively confirming the proper synthesis of MGP composite. Fig. 4(g) demonstrates the distribution of elements within the sample representing the homogeneity of elements.

2.5.6. Transmission Electron Microscopy (TEM) (Supporting grounds)

To further analyze the microstructure of MGP2 composite, its High Resolution TEM analysis was performed. Fig. 5 (a-f) represents the HR-TEM images with Selected Area Electron Diffraction (SAED) pattern of MGP2 composite. MGP2 composite reveals a globular morphology

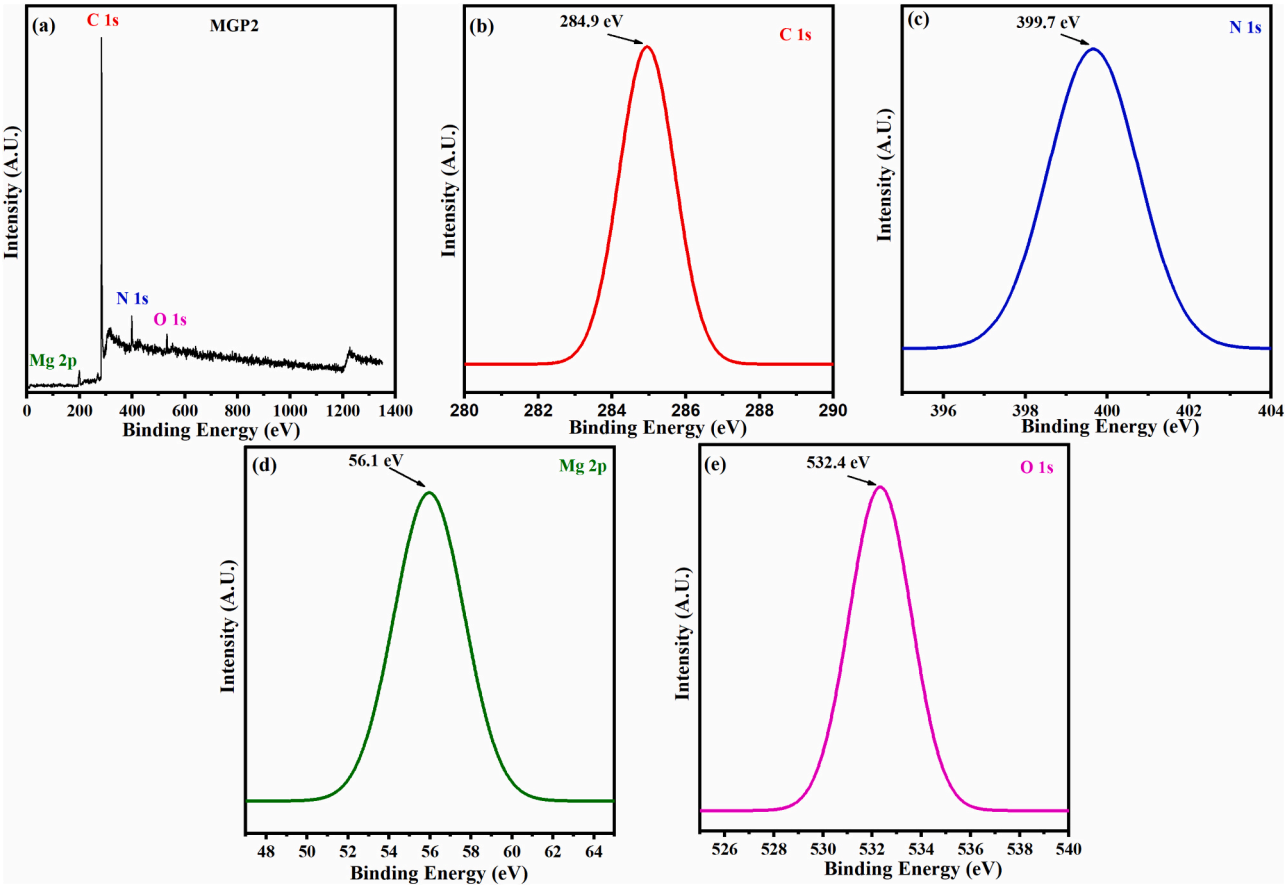

Fig. 6. (a) XPS Survey spectra of MGP2 composite; XPS spectra of (b) C 1 s (c) N 1 s (d) Mg 2p (e) O 1 s.

where the components of composite are densely packed, likely corresponding to MgO and g-C_3N_4 nanoparticles embedded in PPy matrix. The uniform distribution of these globules suggests a homogeneous mixture of the components. The SAED pattern elucidates diffused rings with clear bright spots indicating the semi crystalline nature of composite with some degree of crystallinity due to the presence of MgO nanoparticles which is consistent with the XRD results.

2.5.7. *X-ray Photoelectron Spectroscopy (XPS)*

The oxidation state of elements present in the composite was analyzed by X-ray Photoelectron Spectroscopy performed via ESCA Omicron Nano Technology. Fig. 6(a) displays the XPS survey spectra of MGP2 composite showing the presence of C, N and O. The C 1 s and N 1 s peak are centered at 284.9 eV and 399.7 eV respectively, which indicates the sp^2 hybridized carbon and nitrogen, typically of g-C_3N_4 and PPy. The Mg 2p peak is detected at 56.1 eV in the deep spectra, characteristic of MgO, where magnesium is in +2 oxidation state which is also confirmed by the O 1 s peak at 532.4 eV. The absence of Mg 2p peak in survey spectra indicates that MgO is present in a thin layer within the composite.

2.5.8. *Brunauer-Emmett-Teller (BET)*

The evaluation of specific surface area of MGP composite and its precursors was done through Nova touch LX4 Quanta chrome, Anton PAAR, 2021 BET surface area and pore size analyzer in nitrogen atmosphere at 77 K after degassing the sample for 24 h at 60 °C. Fig. 7(a-c) demonstrates the adsorption-desorption isotherms for g-C_3N_4, PPy and MGP2 revealing a minimum adsorption capacity at low pressure followed by a rapid and pronounced increase in adsorption as pressure increases. Also, a loop like shape is observed in adsorption-desorption isotherm of MGP2 indicating the presence of H_3 type hysteresis with affirmation of type IV isotherm [40]. The pore size and pore volume of synthesized samples calculated from Barreett-Joyner-Halenda (BJH) desorption curve and specific surface area calculated from multi point BET theory are tabulated in Table 1 while the variation of pore volume with pore size is shown in Fig. 7(d-f). The specific surface area of MGP2 composite was obtained as 109.452 $m^2\ g^{-1}$ with pore diameter of 3.053 nm depicting the mesoporous nature of material. The specific surface area of composite surpassed that of its precursors, validating its increased fluffiness morphology, which, in turn, translates to an elevated number of active sites available for adsorption of ions and thus making it a suitable electrode material for Supercapacitors.

2.5.9. *Electrochemical characterizations*

To estimate the performance of MGP composites as supercapacitor electrode material, their electrochemical measurements were performed using Metrohm Autolab potentiostat/galvanostat instrument supported by Nova software. The performance of electrode material was analyzed by pasting approximately 1 mg of slurry on a graphite electrode of thickness 0.5 mm using drop casting method over an area of 1 cm × 1 cm. The electrode material slurry was prepared by mixing active material with acetylene black using DMF as a solvent and PVA as a binder. The ratio of electrode material, acetylene black and binder in slurry preparation was 8: 1: 1. As shown in Fig. 8(a), the electrochemical performance of electrode material was assessed in a 3-electrode system with 1 M H_2SO_4 as electrolyte employing cyclic voltammetry (CV), galvanostatic charge discharge (GCD) and electrochemical impedance spectroscopy (EIS). The reference and counter electrodes were Ag/AgCl and platinum wire, respectively.

After examining the electrochemical properties of electrode material, a hybrid asymmetric supercapacitor device was fabricated using the best composite as cathode and activated charcoal as anode. A Whatman filter

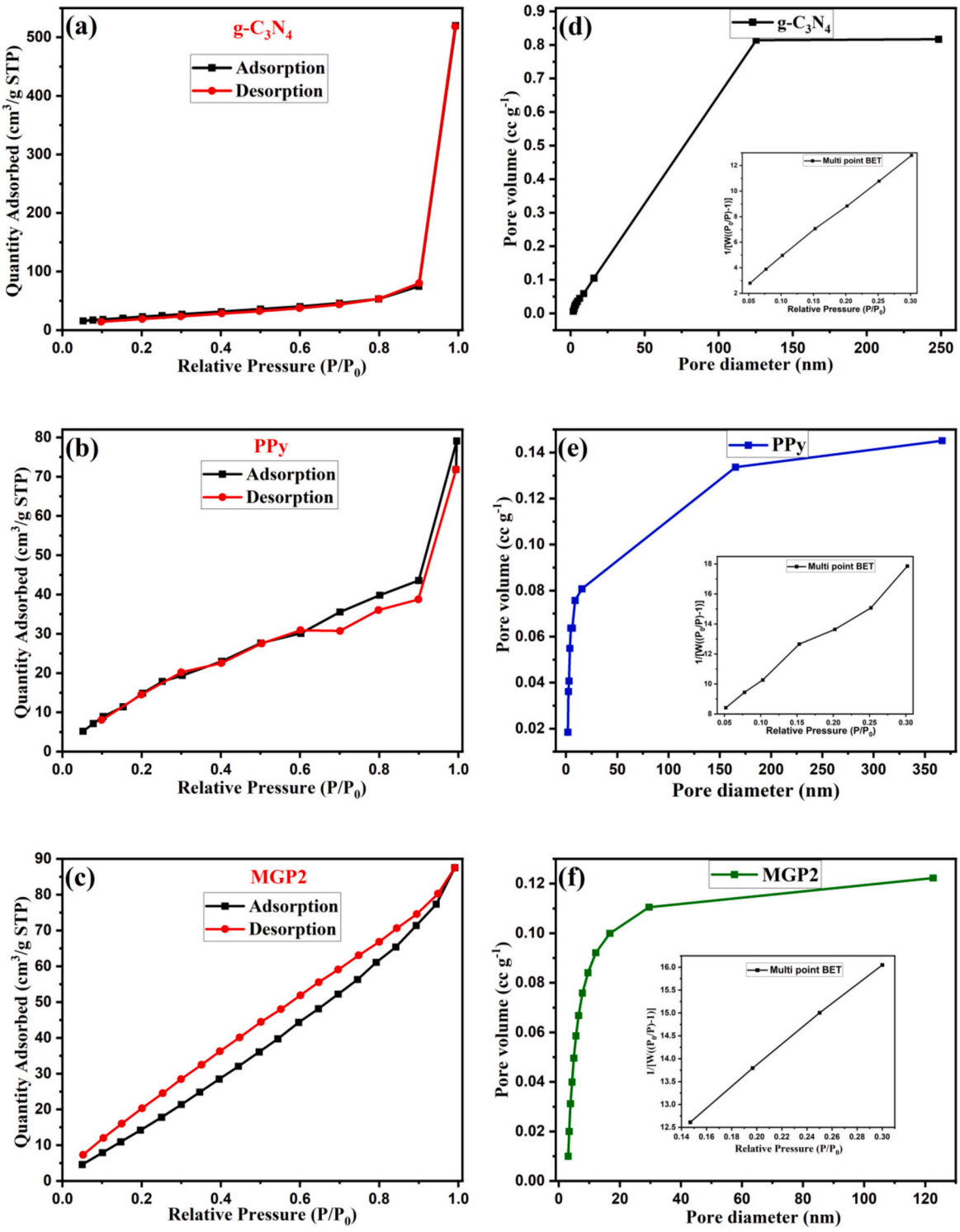

Fig. 7. Adsorption- desorption isotherm of (a) g-C_3N_4 (b) PPy (c) MGP2 and Pore volume variations with pore diameter (d) g-C_3N_4 (e) PPy (f) MGP2 (inset: Langmuir plot).

Table 1
Pore characteristics of synthesized samples.

Sample	Pore volume (cc g^{-1})	Pore diameter (nm)	Specific surface area (m^2 g^{-1})
g-C_3N_4	0.817	2.325	85.896
PPy	0.145	1.809	82.071
MGP2	0.122	3.053	109.452

paper dipped in 1 M H_2SO_4 was used as a separator. The schematic fabrication of device is shown in Fig. 8(b).

To calculate the specific capacitance using CV, GCD and EIS, following equations were used [41,42]

$$Cv = \frac{\int IdV}{m\nu\triangle V} \quad (1)$$

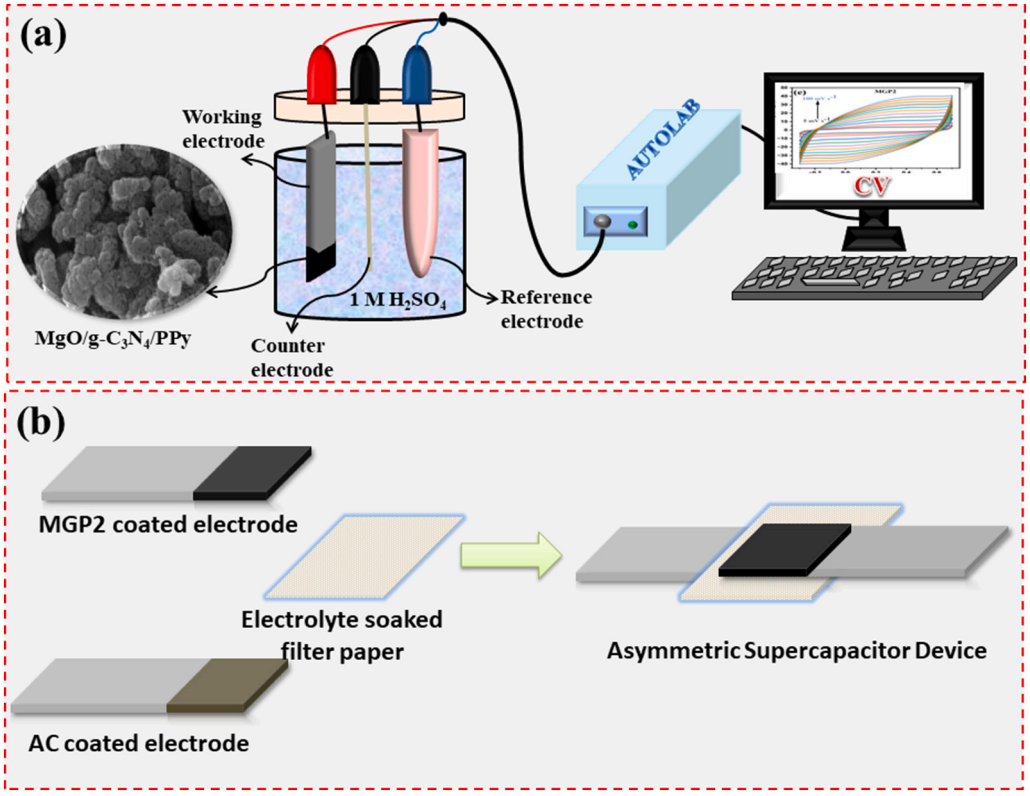

Fig. 8. (a) Schematic representation of a 3-electrode system for electrochemical measurements (b) Schematic illustration of fabrication of device.

$$Cd = \frac{2\,I\int Vdt}{m \times (\triangle v)^2} \tag{2}$$

$$Cs = \frac{-1}{2\pi f z'' m} \tag{3}$$

where C_v, C_d and C_s represents the specific capacitance in F g^{-1} from CV, GCD and EIS data respectively, I represent the current in mA, m shows the mass in mg, ν represents the scan rate in mV s^{-1}, z'' represents the imaginary impedance in ohm at lowest frequency, f is the frequency in Hz and $\triangle V$ represents the potential window of working electrode respectively. The calculation of energy density (E), power density (P) and coulombic efficiency (η) [43,44] was done using Eqs. (4), (5) and (6) in which C represents the specific capacitance from GCD data, t_d and t_c are discharging time and charging time respectively [45,46].

$$E = \frac{1}{2 \times 3.6} \times C_d \times \triangle V^2 \tag{4}$$

$$P = 3600 \times \frac{E}{\triangle t} \tag{5}$$

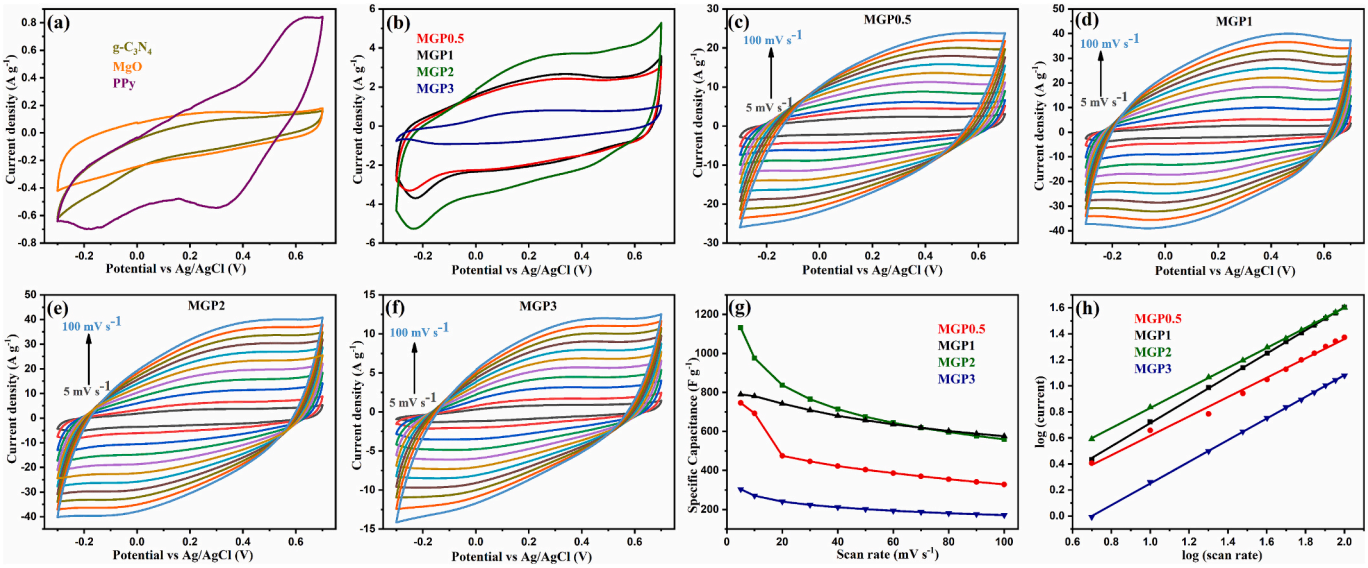

Fig. 9. Cyclic voltammogram of (a) g-C_3N_4, MgO and PPy (b) MGP0.5, MGP1, MGP2 and MGP3 at 5 mV s^{-1}; CV curves at different scan rates for (c) MGP 0.5 (d) MGP1 (e) MGP2 (f) MGP3 (g) Variation of specific capacitance with scan rate for different composites (h) Graph of log(current) vs log(scan rate) for MGP composites.

Table 2
Change in specific capacitance with scan rate for different composites.

Specific capacitance (F g^{-1})				
Scan rate (mV s^{-1})	MGP0.5	MGP1	MGP2	MGP3
5	746.4	790.0	**1132.1**	304.0
10	693.0	781.0	976.4	270.6
20	475.2	743.0	837.5	240.5
30	446.7	709.7	765.3	223.7
40	422.5	680.0	714.2	211.4
50	404.0	657.2	675.6	201.6
60	386.7	636.7	644.5	193.7
70	370.0	619.1	618.8	186.9
80	355.0	602.5	596.7	181.0
90	341.4	588.8	577.2	175.8
100	328.4	575.7	559.8	171.3

Bold letters have been used to highlight the electrochemical parameters obtained for MGP2 composite.

$$\eta = \frac{t_d}{t_c} \times 100 \quad (6)$$

2.5.10. CV, GCD and EIS on 3-electrode setup

To evaluate the kinetics of reaction and elucidate the mechanism of charge storage, CV technique was employed within a potential window spanning from 0.7 V to −0.3 V and scan rate was varied from 5 mV s^{-1} to 100 mV s^{-1}. The analysis of charge storage capacity of different composites was done by comparing the CV curves of MgO, g-C_3N_4, PPy and MGP at 5 mV s^{-1}. It was observed that MGP composites have higher integral area under CV curve and hence specific capacitance than its precursors MgO, g-C_3N_4 and PPy. The specific capacitance calculated using Eq. (1) was 60.64 F g^{-1}, 66.77 F g^{-1}, 162.56 F g^{-1}, 746.46 F g^{-1}, 790.27 F g^{-1}, **1132.12 F g^{-1}** and 242.42 F g^{-1} for MgO, g-C_3N_4, PPy, MGP0.5, MGP1, MGP2 and MGP3 respectively at a scan rate of 5 mV s^{-1}. As can be seen in Fig. 9(a), the CV curve of g-C_3N_4 exhibits a rectangular shape which is indicative of EDLC behavior while the CV curve of PPy shows the presence of redox peaks depicting the pseudocapacitive behavior. CV curve of MGP composites (Fig. 9(b)) also depict reduction peak at lower scan rate indicating a redox reaction between the electrode and electrolyte, while its absence at higher scan rates suggests a kinetic limitation. This may be the result of synergistic effect of EDLC and pseudocapacitance in MGP composites thereby increasing their specific capacitance. The amount of MgO was further optimized by varying its concentration in the previously reported binary composite of g-C_3N_4/PPy [47] and it was observed that on increasing the amount of MgO, a corresponding increase in specific capacitance was observed which could be possible due to the augmentation of available active sites for the effective interaction with the electrolyte ions. However, as the concentration of MgO increased further, the specific capacitance showed a decline which might be ascribed to the covering of active sites of g-C_3N_4 and PPy, thus hindering the charge transfer process. The shape of CV curve of MGP composites is quasi rectangular with the presence of redox peaks representing their pseudocapacitive behavior.

CV curves of MGP composites at various scan rates, Fig. 9(c-f), were explored in order to further anticipate the mechanism of charge storage, whether it be capacitive or battery-based by examining the variation of current (i) with scan rate (ν) as [48]

$$i = a\nu^b \quad (6)$$

Here, the parameter 'b' suggests the kinetics of reaction. Typically, b has two values, b = 0.5 and b = 1. A 'b' value of 0.5 refers to the faradic reactions that occur in the bulk of material (like voids, grain boundaries, pores) [49] and usually represents battery type behavior. While 'b' value of 1 represents the contribution of surface reactions showing EDLC and pseudocapacitive behavior. From Fig. 9(h), the slope of curve gives the value of 'b' which is 0.74, 0.89, 0.77 and 0.83 for MGP0.5, MGP1, MGP2 and MGP3 respectively showing the more contribution of surface than bulk and hence representing more contribution of pseudocapacitance in MGP composites. As the scan rate is increased, the interaction of electrolyte ions and pores of electrode material are restricted by time constraint resulting in reduced specific capacitance of electrode material as shown in Fig. 9(g). The shape of CV curve remained almost same with varying scan rate depicting the fast faradic reaction in electrodes [50].

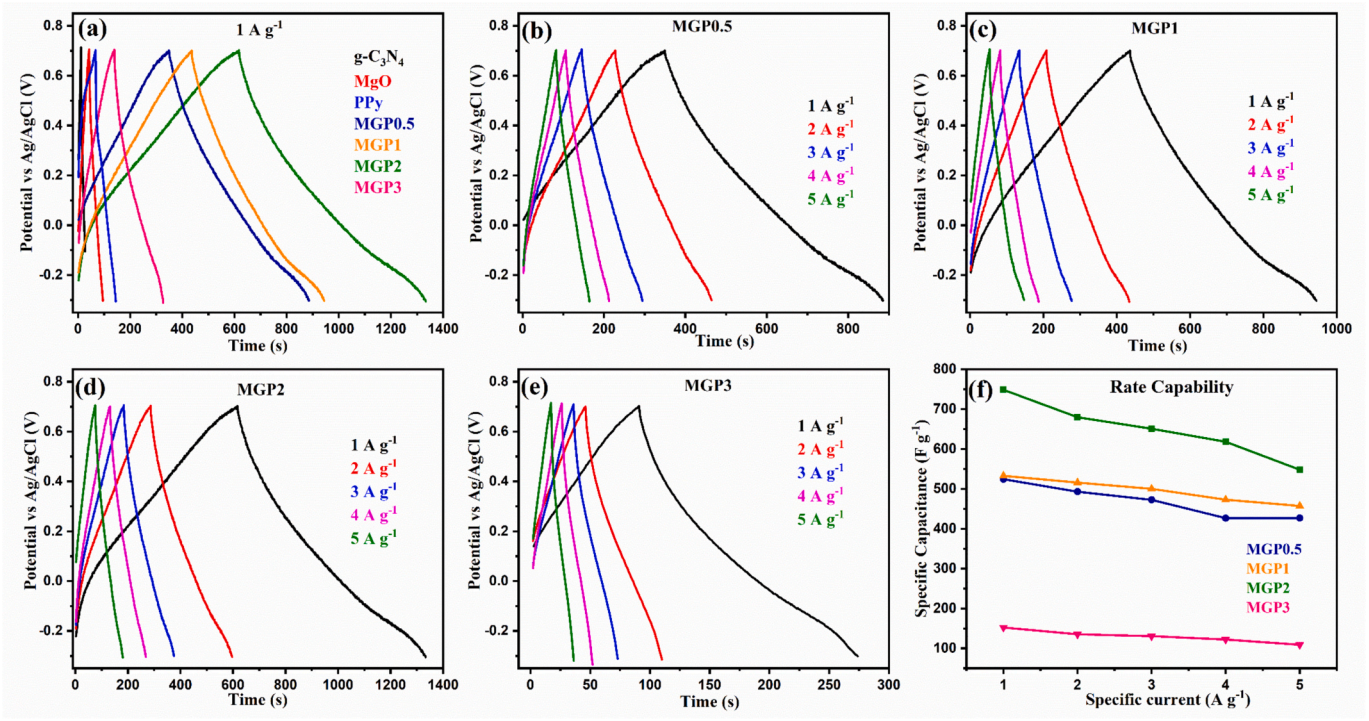

Fig. 10. (a) GCD graphs of g-C_3N_4, MgO, PPy, MGP0.5, MGP1, MGP2 and MGP3 at 1 A g^{-1}; GCD graphs at different current densities for (b) MGP0.5 (c) MGP1 (d) MGP2 (e) MGP3; (f) Rate capability of different composites.

Table 3
Variation of specific capacitance with current density for different composites.

Specific capacitance (F g^{-1})				
Current density (A g^{-1})	MGP0.5	MGP1	MGP2	MGP3
1	524.32	532.58	**748.34**	152.62
2	493.07	515.90	679.80	135.28
3	472.72	500.10	650.76	130.96
4	426.56	472.88	618.24	122.10
5	426.82	457.34	548.05	109.27

Table 2 illustrates the specific capacitance of MGP composites at different scan rate.

To get more insights into electrochemical behavior of MGP composites, GCD technique was employed in the same electrolyte and potential window by applying a constant current and measuring the corresponding voltage response (Fig. 10(a)). The value of specific capacitance from GCD calculated using Eq. (2) was 16.40 F g^{-1}, 54.48 F g^{-1}, 102.07 F g^{-1}, 524.32 F g^{-1}, 532.58 F g^{-1}, **748.34 F g^{-1}** and 152.62 F g^{-1} for g-C_3N_4, MgO, PPy, MGP0.5, MGP1, MGP2 and MGP3 respectively at a current density of 1 A g^{-1}. The rate capability of reaction was analyzed for MGP2 by varying the applied current and noting the corresponding voltage response (Fig. 10(b-e)). It was noted that as the specific current was increased, both the discharge duration and, consequently, the specific capacitance decreased. This phenomenon can likely be attributed to the constrained ion diffusion kinetics at elevated current densities, leading to an incomplete charging or discharging of the electric double layer within the specified time frame. Table 3 represents the specific capacitance values at various current densities.

Further electrochemical analysis of the samples, including the assessment of parameters such as charge transfer resistance and solution resistance, was carried out through EIS measurement in the frequency range from 0.1 Hz to 10^5 Hz. Fig. 11(a-b) represents the Nyquist plot of MgO, g-C_3N_4, PPy, MGP0.5, MGP1, MGP2 and MGP3. Notably, the absence of semi-circle in high frequency region of Nyquist plot demonstrates the lower value of charge transfer resistance [51]. Meanwhile, in the low-frequency region for the MGP composites, the presence of a "finite space Warburg impedance" demonstrates capacitive behavior [52]. To obtain the value of charge transfer resistance (R_{ct}) across electrode-electrolyte interface and solution resistance (R_s) between working electrode and electrolyte, an equivalent electrochemical circuit

Table 4
Solution resistance, charge transfer resistance and specific capacitance from EIS data.

Sample	R_s (ohm)	R_{ct} (ohm)	Specific capacitance (F g^{-1})
g-C_3N_4	5.2	3.5	38.83
MgO	2.8	1.5	29.54
PPy	1.2	3.5	46.79
MGP0.5	1.2	0.7	83.15
MGP1	1.0	1.3	111.17
MGP2	0.7	0.6	112.56
MGP3	1.2	1.5	71.82

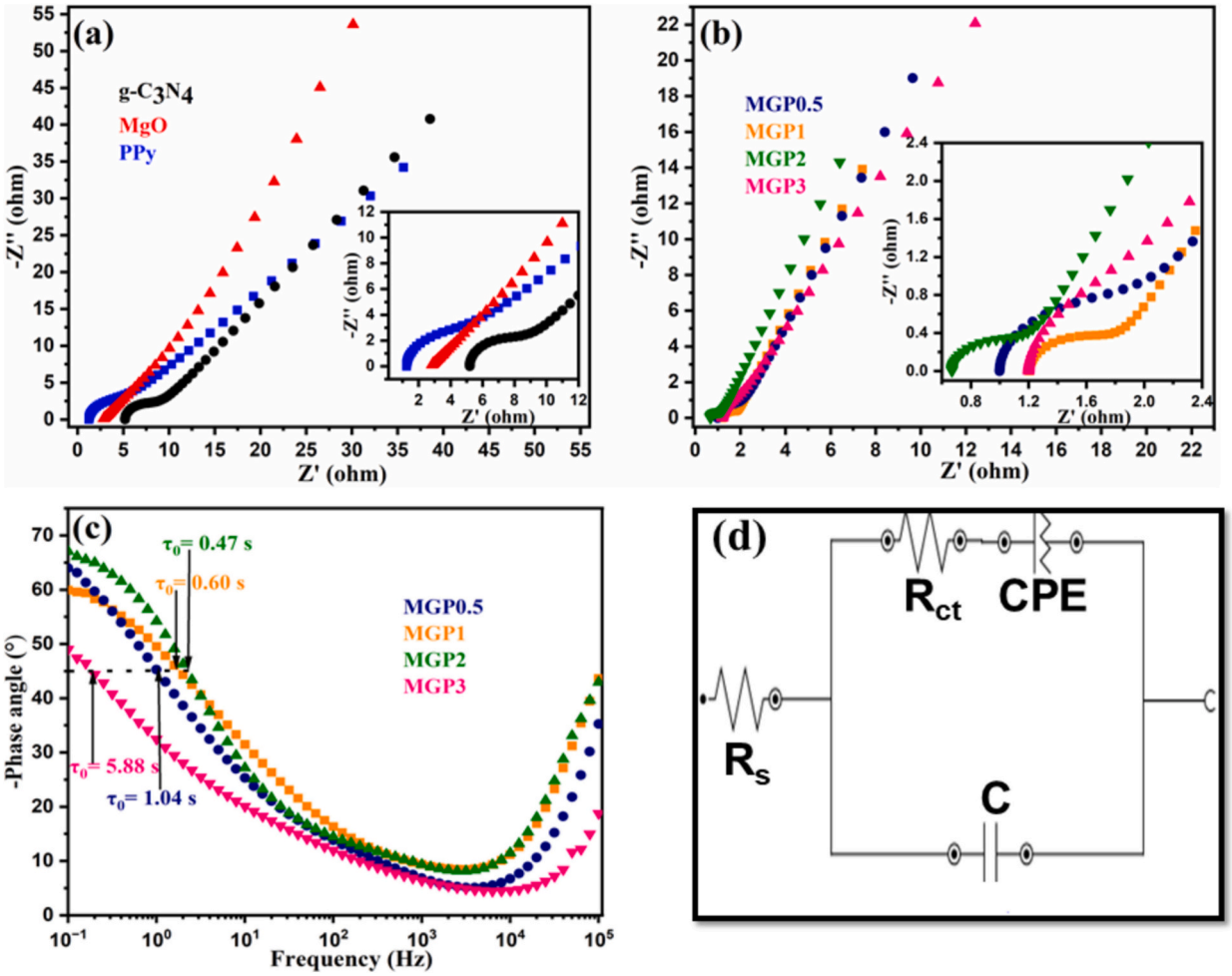

Fig. 11. Nyquist plot of (a) g-C_3N_4, MgO and PPy (b) MGP0.5, MGP1, MGP2 and MGP3 (inset: magnified view of high frequency region) (c) Bode plot of MGP composites (d) Equivalent electrochemical circuit for fitting of EIS data.

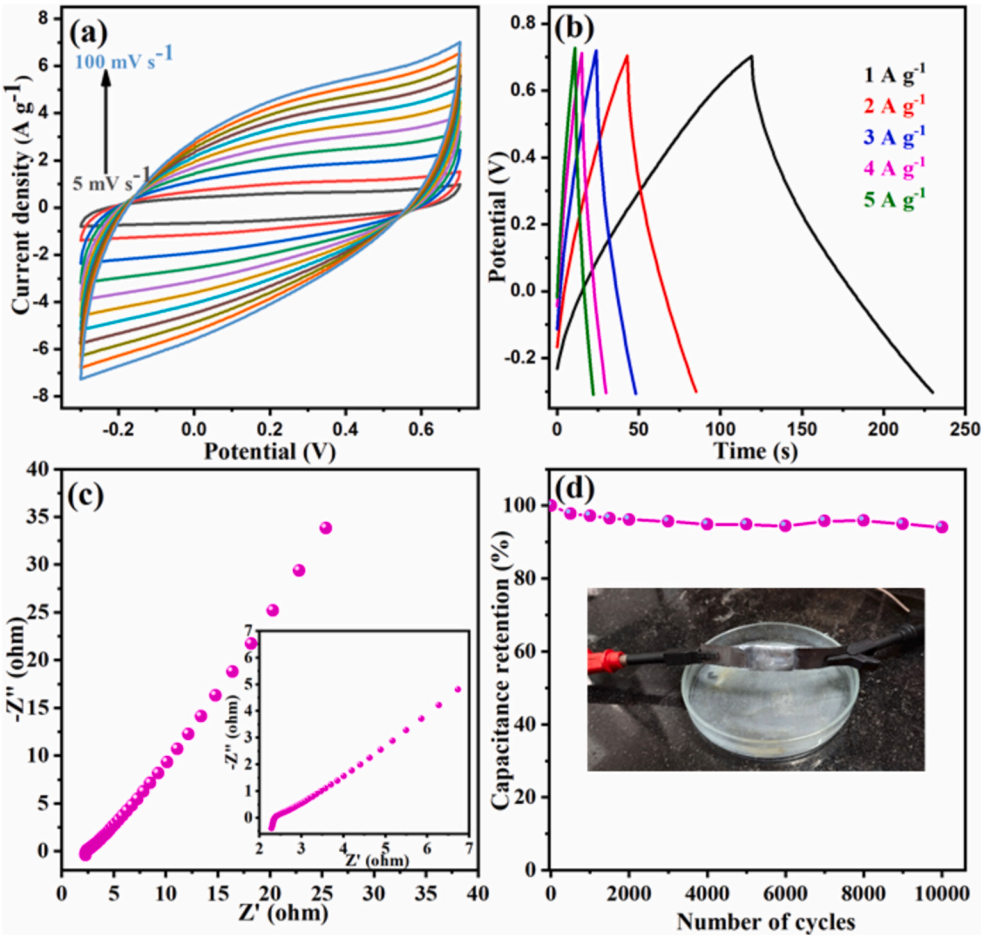

Fig. 12. (a) CV curve of asymmetric supercapacitor device at different scan rate (b) GCD curve of asymmetric supercapacitor device at different current density (c) Nyquist plot of asymmetric supercapacitor device in the frequency range from 10^5 Hz to 0.1 Hz (d) Variation of capacitance retention with number of cycles (inset: image of asymmetric supercapacitor device).

Table 5
Change in specific capacitance with scan rate for ASD.

Scan rate (mV s^{-1})	Specific capacitance (F g^{-1})
5	103.22
10	87.03
20	71.72
30	63.29
40	57.43
50	53.12
60	49.75
70	47.02
80	44.61
90	42.64
100	40.94

(Fig. 11(d)) was fitted for all the samples and the values are shown in Table 4 where specific capacitance was calculated using Eq. (3). In addition, a graph between frequency and phase angle (also known as Bode plot) was also plotted (Fig. 11(c)). The value of time constant which is defined as the reciprocal of frequency where resistance and reactance have equal magnitude i.e. 45^0 was determined to be 1.04 s, 0.60 s, 0.47 s and 5.88 s for MGP0.5, MGP1, MGP2 and MGP3 respectively. Lower values of time constant represents the faster movement of ions between electrode and electrolyte leading to better electrochemical properties of MGP2 composite than other composites [53].

Table 6
Variation of specific capacitance with current density for ASD.

Current density (A g^{-1})	Specific capacitance (F g^{-1})	Coulombic efficiency (%)
1	66.59	92.44
2	48.66	95.35
3	42.45	95.83
4	36.19	93.33
5	34.21	90.91

Table 7
Comparison of energy density and power density of MGP2 composite with previously reported materials in 2-electrode system.

Electrode material	Energy density (W h kg^{-1})	Power density (W kg^{-1})	Reference
PPy/rGO	6.5	80	[55]
MXene/NCF	8.75	1871	[56]
PPy/CNT	9.23	61.31	[57]
M doped Graphene	2.5	1000	[58]
MoS_2/MWCNT/PPy	7.33	119.99	[59]
Co_3O_4@Co/N-CNTs	4.9	5000	[60]
Ag/g-C_3N_4@PPy	5.91	161	[46]
MgO/g-C_3N_4/PPy	**9.25**	**302.72**	**This work**

Bold letters have been used to highlight the electrochemical parameters obtained for MGP2 composite.

2.5.11. Asymmetric supercapacitor device (ASD)

To check the practical applicability of synthesized composites, electrochemical properties of asymmetric supercapacitor device were tested in same conditions as of 3-electrode measurements. Fig. 12(a) demonstrates the CV curve of ASD at varied scan rate. The value of specific capacitance of ASD evaluated using Eqs. (1) and (2) in which m is taken to be the mass deposited on both electrodes, is tabulated in Table 5 and Table 6. A maximum specific capacitance of 103.22 F g^{-1} is obtained at 5 mV s^{-1} for ASD. It is also noted that with increasing scan rate, the value of specific capacitance decreases which is consistent with the 3-electrode measurements. The energy density and power density of ASD was evaluated using Eqs. (4) and (5). The energy density of 9.25 W h kg^{-1} was obtained at a power density of 302.72 W kg^{-1} which is better than the previously reported energy densities of device. A comparison of these parameters with the previously reported literature are shown in Table 7.

The ASD was tested for its cyclic stability by performing 10,000 CV cycles. The assembled device retained 94.03 % specific capacitance after 10,000 cycles showing its remarkable capability to be used in future supercapacitor applications [54]. The coulombic efficiency (η) of device was evaluated using Eq. (6).

2.6. Proposed charge storage mechanism

The enhanced electrochemical performance of MGP2 composite relative to its precursors could be attributed to several key factors such as the layered structure of g-C_3N_4 where the presence of MgO nanoparticles facilitates the ion diffusion allowing for rapid transfer of ions to the active sites. Moreover, during in-situ polymerization, the presence of MgO/g-C_3N_4 composite provides nucleation sites for pyrrole monomers to attach and initiate the polymerization leading to modified globular structure of MGP composite with increased fluffiness. In addition, the incorporation of PPy leads to the introduction of redox active sites, such as nitrogen containing groups aiding reversible redox reactions during charging and discharging cycles. The better performance of MGP2 composite over other composites arises from the constrained nucleation sites in MgO/g-C_3N_4 matrix impeding the charge transfer and hence reduced electrochemical performance with higher concentrations of MgO.

Extensive research is focused on developing the materials which possesses supercapacitive properties. Thus, in order to demonstrate the superiority of this work, the energy density of MGP2 composite with other previously reported materials is compared in Table 7.

3. Conclusion

In summary, MgO/g-C_3N_4/PPy composite was synthesized through calcination route followed by in-situ polymerization. The investigation focused on optimizing the electrochemical performance by varying the content of MgO. Notably, MGP2 composite exhibited a remarkable specific capacitance of 1132.12 F g^{-1} when assessed in 3-electrode cell at a scan rate of 5 mV s^{-1} in 1 M H_2SO_4. The specific capacitance of various composites and their precursors was also assessed using GCD and EIS data, revealing a similar trend. The proper synthesis of composites was confirmed by XRD, FTIR and Raman spectroscopy. Morphological analysis through FESEM revealed alterations in globular type morphology of PPy exhibiting augmented fluffiness. This was further supported by BET analysis where the specific surface area of MGP2 composite was found to be 109.452 m^2 g^{-1} significantly more than its antecedents facilitating increased active sites for adsorption and desorption of ions and consequently better electrochemical properties thereby making MGP2 composite a potential electrode material for future supercapacitor applications.

CRediT authorship contribution statement

Manisha: Writing – review & editing, Writing – original draft, Project administration, Methodology, Investigation, Funding acquisition, Formal analysis, Conceptualization. **Monika Dhanda:** Writing – review & editing, Investigation, Formal analysis. **Varij Panwar:** Writing – review & editing, Resources, Methodology, Conceptualization, Data curation. **Suman Lata:** Writing – review & editing, Resources, Conceptualization. **Harish Kumar:** Writing – review & editing, Resources, Conceptualization. **Anshu Sharma:** Writing – review & editing, Visualization, Supervision, Resources, Project administration, Funding acquisition, Conceptualization.

Declaration of competing interest

The authors declare that they have no known competing financial interests or personal relationships that could have appeared to influence the work reported in this paper.

Acknowledgements

The Council of Scientific and Industrial Research (CSIR) is commended for providing Junior Research Fellowship (Ref. No. 16/06/2019 (i) EU-V) to Manisha. AS is highly thankful to Science and Engineering Board (SERB), Department of Science and Technology (DST), Government of India for providing research funding under the SERB University Research Excellence (SURE) scheme (File No. SUR/2022/004191).

Data availability

Data will be made available on request.

References

[1] Y. Mao, J. Xie, H. Liu, W. Hu, Hierarchical core-shell ag@Ni(OH)2@PPy nanowire electrode for ultrahigh energy density asymmetric supercapacitor, Chem. Eng. J. 405 (2021) 126984.
[2] H. Ibrahim, A. Ilinca, J. Perron, Energy storage systems-characteristics and comparisons, Renew. Sust. Energ. Rev. 12 (2008) 1221–1250.
[3] L. Sun, Y. Gong, D. Li, C. Pan, Biomass-derived porous carbon materials: synthesis, designing, and applications for supercapacitors, Green Chem. 24 (2022) 3864–3894.
[4] J. Wang, et al., Symmetric supercapacitors composed of ternary metal oxides (NiO/V2O5/MnO2) nanoribbon electrodes with high energy storage performance, Chem. Eng. J. 426 (2021).
[5] C. Bora, J. Sharma, S. Dolui, Polypyrrole/sulfonated graphene composite as electrode material for supercapacitor, J. Phys. Chem. C 118 (2014) 29688–29694.
[6] S. Kumar, et al., 0D to 3D carbon-based networks combined with pseudocapacitive electrode material for high energy density supercapacitor: a review, Chem. Eng. J. 403 (2021) 126352.
[7] F. Rafik, H. Gualous, R. Gallay, A. Crausaz, A. Berthon, Frequency, thermal and voltage supercapacitor characterization and modeling, J. Power Sources 165 (2007) 928–934.
[8] G.M. Tomboc, et al., Carbon transition-metal oxide electrodes: understanding the role of surface engineering for high energy density supercapacitors, Chem. - An Asian J. 15 (2020) 1628–1647.
[9] S. Kulandaivalu, N. Suhaimi, Y. Sulaiman, Unveiling high specific energy supercapacitor from layer-by-layer assembled polypyrrole/graphene oxide| polypyrrole/manganese oxide electrode material, Sci. Rep. 9 (2019) 1–10.
[10] Y. Wang, Z. Chang, M. Qian, T. Lin, F. Huang, A bridge between battery and supercapacitor for power/energy gap by using dual redox-active ions electrolyte, Chem. Eng. J. 375 (2019) 122054.
[11] M. Dhanda, R. Arora, S. Ahlawat, S.P. Nehra, S. Lata, Electrolyte as a panacea to contemporary scientific world of super-capacitive energy: a condense report, J. Energy Storage 52 (2022) 104740.
[12] M. Pershaanaa, S. Bashir, S. Ramesh, K. Ramesh, Every bite of Supercap: a brief review on construction and enhancement of supercapacitor, J. Energy Storage 50 (2022) 104599.
[13] H. Sun, et al., Unveiling the key factors affecting the grain size of NiCo2O4 during electrodeposition, Appl. Surf. Sci. 606 (2022) 154899.
[14] D.P. Dubal, S.H. Lee, J.G. Kim, W.B. Kim, C.D. Lokhande, Porous polypyrrole clusters prepared by electropolymerization for a high performance supercapacitor, J. Mater. Chem. 22 (2012) 3044–3052.
[15] H. Zhu, S. Peng, W. Jiang, Electrochemical properties of PANI as single electrode of electrochemical capacitors in acid electrolytes, Sci. World J. 2013 (2013).

[16] C. Xu, et al., Controllable Design of Polypyrrole-Iron Oxide Nanocoral Architectures for supercapacitors with ultrahigh cycling stability, ACS Appl. Energy Mater. 2 (2019) 2161–2168.
[17] Y. Fan, et al., PANI-Co3O4 with excellent specific capacitance as an electrode for supercapacitors, Ceram. Int. 47 (2021) 8433–8440.
[18] D. Zhang, et al., Enhanced capacitance and rate capability of graphene/polypyrrole composite as electrode material for supercapacitors, J. Power Sources 196 (2011) 5990–5996.
[19] A. Aphale, K. Maisuria, M.K. Mahapatra, A. Santiago, Hybrid electrodes by in-situ integration of graphene and carbon-nanotubes in Polypyrrole for supercapacitors, Nat. Publ. Gr. 1–8 (2015), https://doi.org/10.1038/srep14445.
[20] A. Moyseowicz, A. Śliwak, E. Miniach, G. Gryglewicz, Polypyrrole/iron oxide/reduced graphene oxide ternary composite as a binderless electrode material with high cyclic stability for supercapacitors, Compos. Part B Eng. 109 (2017) 23–29.
[21] H. Abdalla, et al., Vanadium-doped magnesium oxide nanoparticles as electrodes in supercapacitor devices, J. Alloys Compd. 958 (2023) 170442.
[22] L. Song, M. Liya, S. Xinyu, T. Hua, Potassium chloride-catalyzed growth of porous carbon nanotubes for high-performance supercapacitors, J. Alloys Compd. 906 (2022) 164242.
[23] K. Karthikeyan, S. Amaresh, V. Aravindan, Y.S. Lee, Microwave assisted green synthesis of MgO-carbon nanotube composites as electrode material for high power and energy density supercapacitors, J. Mater. Chem. A 1 (2013) 4105–4111.
[24] K. Kalidasan, et al., Transition metals-doped g-C3N4 nanostructures as advanced photocatalysts for energy and environmental applications, Chemosphere 352 (2024) 141354.
[25] J. Madona, C. Sridevi, Surfactant assisted hydrothermal synthesis of MgO/g-C3N4 heterojunction nanocomposite for enhanced solar photocatalysis and antimicrobial activities, Inorg. Chem. Commun. 138 (2022) 109265.
[26] R. Dubey, V. Guruviah, Review of carbon-based electrode materials for supercapacitor energy storage, Ionics (Kiel) 25 (2019) 1419–1445.
[27] K. Ishii, K. Sato, Y. Oaki, H. Imai, Highly porous polymer dendrites of pyrrole derivatives synthesized through rapid oxidative polymerization, Polym. J. 51 (2019) 11–18.
[28] N.H.N. Azman, Mamat @ Mat Nazir, M. S., Ngee, L. H. & Sulaiman, Y., Graphene-based ternary composites for supercapacitors, Int. J. Energy Res. 42 (2018) 2104–2116.
[29] M. Zhang, hui, Chen, X. & Dong, H., A study on multistep thermal decomposition behavior and kinetics of magnesium nitrate hydrate, Thermochim. Acta 701 (2021) 178951.
[30] D. Rattan Paul, S.P. Nehra, Graphitic carbon nitride: a sustainable photocatalyst for organic pollutant degradation and antibacterial applications, Environ. Sci. Pollut. Res. 28 (2021) 3888–3896.
[31] D.R. Paul, et al., Mg/Li@GCN as highly active visible light responding 2D photocatalyst for wastewater remediation application, Environ. Sci. Pollut. Res. 3–10 (2022), https://doi.org/10.1007/s11356-022-21203-z.
[32] E.R. Essien, V.N. Atasie, A.O. Okeafor, D.O. Nwude, Biogenic synthesis of magnesium oxide nanoparticles using Manihot esculenta (Crantz) leaf extract, Int. Nano Lett. 10 (2020) 43–48.
[33] D.R. Paul, et al., ZnO-modified g-C3N4: a potential Photocatalyst for environmental application, ACS Omega 5 (2020) 3828–3838.
[34] S. Pareek, M. Sharma, S. Lal, J.K. Quamara, Polymeric graphitic carbon nitride–barium titanate nanocomposites with different content ratios: a comparative investigation on dielectric and optical properties, J. Mater. Sci. Mater. Electron. 29 (2018) 13043–13051.
[35] Y. Wei, et al., One-step UV-induced synthesis of Polypyrrole/ag nanocomposites at the water/ionic liquid Interface, Nanoscale Res. Lett. 5 (2010) 433–437.
[36] N.M.A. Hadia, H.A.H. Mohamed, Characteristics and optical properties of MgO nanowires synthesized by solvothermal method, Mater. Sci. Semicond. Process. 29 (2015) 238–244.
[37] L. Ge, et al., G-C3N4/MgO nanosheets: light-independent, metal-poisoning-free catalysts for the activation of hydrogen peroxide to degrade organics, J. Mater. Chem. A 6 (2018) 16421–16429.
[38] S. Rsoniya, V.M. Nair, Synthesis and characterization of nanostructured mg(OH)2 and MgO, Int. J. Sci. Res. 5 (2016) 197–203.
[39] Dhanda, M., Arora, R., Saini, M., Nehra, S. P. & Lata, S. Prolific intercalation of VO2 (D)/polypyrrole/g-C3N4 as an energy storing electrode with remarkable capacitance. 14251–14266 (2022) doi:https://doi.org/10.1039/d2nj02401b.
[40] M. Pathak, et al., Few layer graphene nanosheets from kinnow peel waste for high-performance supercapacitors: a comparative study with three different electrolytes, J. Energy Storage 55 (2022) 105729.
[41] A. Balducci, D. Belanger, T. Brousse, J.W. Long, W. Sugimoto, Perspective—a guideline for reporting performance metrics with electrochemical capacitors: from electrode materials to full devices, J. Electrochem. Soc. 164 (2017) A1487–A1488.
[42] Manisha, et al., Coalescing of lanthanum oxide and PPy @graphitic carbon nitride to achieve ultrahigh energy density electrode material for supercapacitors applications, J. Alloys Compd. 955 (2023) 169738.
[43] C. Sambathkumar, N. Nallamuthu, M.K. Kumar, S. Sudhahar, P. Devendran, Electrochemical exploration of cobalt sulfide nanoparticles synthesis using cobalt diethyldithiocarbamate as single source precursor for hybrid supercapacitor device, J. Alloys Compd. 920 (2022) 165839.
[44] M. Murugesan, K.R. Nagavenkatesh, N. Nallamuthu, P. Devendran, K. Ramesh, Electrochemical investigation of orthorhombic structured Mg3(VO4)2 nanoparticles modified estimable electrode for high dense energy devices, J. Energy Storage 89 (2024).
[45] R. Abazari, S. Sanati, A. Morsali, D.P. Dubal, High specific capacitance of a 3D-metal-organic framework-confined growth in CoMn2O4nanostars as advanced supercapacitor electrode materials, J. Mater. Chem. A 9 (2021) 11001–11012.
[46] R. Arora, S.P. Nehra, S. Lata, Trio obtainment through polypyrrole insertions in argentum/graphitic carbon nitride for accelerating super-capacitive energy parameters, J. Energy Storage 56 (2022) 105879.
[47] R. Arora, S. Pal, N. Suman, In - situ composited g - C 3 N 4 / polypyrrole nanomaterial applied as energy - storing electrode with ameliorated super - capacitive performance, Environ. Sci. Pollut. Res. (2022), https://doi.org/10.1007/s11356-022-21777-8.
[48] J. Liu, et al., Advanced energy storage devices: basic principles, analytical methods, and rational materials design, Adv. Sci. 5 (2018).
[49] B. Pandit, D.P. Dubal, P. Gómez-Romero, B.B. Kale, B.R. Sankapal, V2O5 encapsulated MWCNTs in 2D surface architecture: complete solid-state bendable highly stabilized energy efficient supercapacitor device, Sci. Rep. 7 (2017).
[50] S. Ishaq, et al., Facile synthesis of ternary graphene nanocomposites with doped metal oxide and conductive polymers as electrode materials for high performance supercapacitors, Sci. Rep. 9 (2019) 1–11.
[51] C. Sambathkumar, et al., Electrochemical exploration on hexadecylamine capped copper sulfide nanocubes using single source precursor for enhanced supercapacitor devices, J. Energy Storage 56 (2022) 105898.
[52] N.O. Laschuk, E.B. Easton, O.V. Zenkina, Reducing the resistance for the use of electrochemical impedance spectroscopy analysis in materials chemistry, RSC Adv. 11 (2021) 27925–27936.
[53] C. Yang, et al., Tailoring the supercapacitive behaviors of co / Zn-ZIF derived nanoporous carbon via incorporating transition metal species : a hybrid experimental-computational exploration, Chem. Eng. J. 419 (2021) 129636.
[54] K.R. Nagavenkatesh, et al., Comparative electrochemical investigation for scheelite structured metals tungstate (MWO4 (M = Ni, cu and co)) nanocubes for high dense supercapacitors application, J. Energy Storage 79 (2024) 110153.
[55] A. Moyseowicz, G. Gryglewicz, High-performance hybrid capacitor based on a porous polypyrrole/reduced graphene oxide composite and a redox-active electrolyte, Electrochim. Acta 354 (2020).
[56] L. Sun, G. Song, Y. Sun, Q. Fu, C. Pan, MXene/N-doped carbon foam with three-dimensional hollow neuron-like architecture for freestanding, highly compressible all solid-state supercapacitors, ACS Appl. Mater. Interfaces 12 (2020) 44777–44788.
[57] R. Ullah, et al., Preparation of electrochemical supercapacitor based on Polypyrrole/gum Arabic composites, Polymers (Basel) 14 (2022).
[58] G. Tatrari, et al., Mass production of metal-doped graphene from the agriculture waste of Quercus ilexleaves for supercapacitors: inclusive DFT study, RSC Adv. 11 (2021) 10891–10901.
[59] N. Jhanjhariya, S. Lata, Potential window optimization to upgrade the performance of the designed triad MoS2/MWCNT/PPy as an asymmetric supercapacitor device, J. Energy Storage 82 (2024) 110577.
[60] S.V. Mulik, et al., Square-facet Nanobar MOF-derived Co3O4@co/N-doped CNT Core-Shell-based nanocomposites as cathode materials for high-performance supercapacitor studies, ACS Omega (2022), https://doi.org/10.1021/acsomega.2c06369.